Soft Matter

Pressure-driven occlusive flow of a confined red blood cell†

Thierry Savin,‡[a] M. M. Bandi§[a] and L. Mahadevan*[ab]

When red blood cells (RBCs) move through narrow capillaries in the microcirculation, they deform as they flow. In pathophysiological processes such as sickle cell disease and malaria, RBC motion and flow are severely restricted. To understand this threshold of occlusion, we use a combination of experiment and theory to study the motion of a single swollen RBC through a narrow glass capillary of varying inner diameter. By tracking the movement of the squeezed cell as it is driven by a controlled pressure drop, we measure the RBC velocity as a function of the pressure gradient as well as the local capillary diameter, and find that the effective blood viscosity in this regime increases with both decreasing RBC velocity and tube radius by following a power-law that depends upon the length of the confined cell. Our observations are consistent with a simple elasto-hydrodynamic model and highlight the role of lateral confinement in the occluded pressure-driven slow flow of soft confined objects.

I. Introduction

The microcirculatory network of blood vessels in the body primarily serves as the conduit for the exchange of gases between blood and tissues, through the red blood cells (RBCs).[1] It is composed of arterioles, capillaries and venules whose diameters range from about 3 μm to about 200 μm. Many studies on the associated confined flow of blood have been performed *in vivo*[2,3] and *in vitro*.[4–6] The measurements particularly focus on the apparent viscosity μ_a of blood at these microscopic scales,[7] with dependence on the inner diameter of the tube $2r$, the tube hematocrit H_T, mechanical properties of the cells, and the mean flow velocity $\bar{v}$ of the surrounding plasma. For healthy blood, μ_a progressively diminishes with decreasing tube size (the Fåhræus–Lindqvist effect) until $2r = 7$ μm, below which it increases sharply.[7] To understand this non-linear rheology, blood must be modelled as a suspension of soft objects rather than a homogeneous fluid. Hence, non-uniform concentration of cells across the tube section in the microcirculating blood explains the changes of μ_a in capillaries wider than 7 μm. Around this value, corresponding to the size of a RBC, the flow is strongly conditioned by the shape and deformability of the

individual cell,[1,8] which can be seen adopting various morphologies: discocyte, slipper, parachute…[4,6,9–11] The geometrical and mechanical properties of individual RBCs have been extensively studied under various experimental conditions,[12–14] and the loss of RBC deformability can notably lead to vaso-occlusion in the microcirculation,[15] and is indeed believed to be a cause for pathological conditions arising in sickle cell anemia[16] and severe malaria.[17,18]

When the RBC diameter ($2a \approx 7$ μm) exceeds the inner diameter $2r$ of the smallest vessels ($4 \leq 2r \leq 8$ μm), like the case that is the focus of the present study, the RBCs must deform to fit into the lumen, and travel in file through capillaries. For a typical tube hematocrit $H_T \in [20\%,40\%]$ found in the microcirculation,[2] cell–cell hydrodynamic interactions may be neglected and the apparent viscosity scales linearly with the number of cells flowing aligned in the capillary segment.[19] Following the arguments of Secomb *et al.*,[9] we may then express μ_a as a linear function of the tube hematocrit H_T, $\mu_a = \mu(1 + K_T H_T)$, where μ is the plasma viscosity. Here K_T is called the apparent intrinsic viscosity, determined at the level of a single cell in the tube, and its assessment suffices to describe the capillary rheology of blood. The apparent viscosity μ_a is, by definition, the effective viscosity of a Newtonian fluid that flows in the capillary with the same velocity under the same imposed pressure gradient. Large values of μ_a indicate occlusive flow and correspond to high K_T. At a single cell level, this definition translates into a local version of Poiseuille's law, $K_T \sim \dfrac{1}{\mu} \dfrac{\delta r^2}{\bar{v} \ell}$, for a longitudinal driving pressure drop δ across a moving cell of length ℓ (see Fig. 1A).[20]

Previous experiments have shown that K_T increases with the decrease in both blood velocity and capillary inner diameter.[19]

[a] *Paulson School of Engineering and Applied Sciences, Harvard University, Cambridge, MA 02138, USA. E-mail: lm@seas.harvard.edu*
[b] *Department of Physics, Harvard University, Cambridge, MA 02138, USA*
† Electronic supplementary information (ESI) available. See DOI: 10.1039/c5sm01282a
‡ Current address: Department of Engineering, University of Cambridge, Cambridge CB2 1PZ, UK.
§ Current address: Collective Interactions Unit, OIST Graduate University, 1919-1 Tancha, Onna-son, Okinawa 904-0495, Japan.
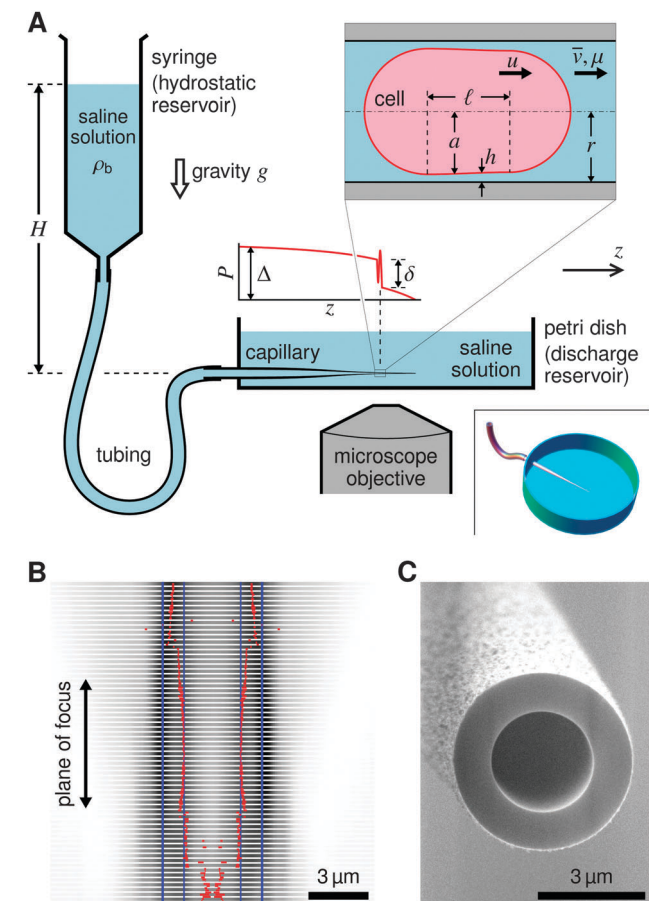
Fig. 1 (A) Schematic of the experimental flow device: a tapered cylindrical capillary (wide-end inner diameter 0.58 mm, tapered tip inner diameter 2 μm) was chemically treated with a tri-block surfactant to inhibit RBC adhesion to its inner wall. The capillary was inserted through a hole into a Petri-dish side and sealed (see 3D view of the bottom-right inset). The Petri dish was filled with 0.5× PBS. RBCs suspended in 0.5× PBS solution were introduced into the capillary. The flow of the RBC was controlled *via* a hydrostatic head whose height was adjusted with a motorized linear translation stage. It produced a driving pressure whose qualitative profile in the capillary is also sketched here. The top-right inset shows the flow geometric parameters (see Table 1 in the Appendix) around the RBC. (B) Inner diameter measurements of the capillary (red points) as determined through image analysis of bright field micrographs, acquired at various planes of focus, as compared to the diameters measured from scanning electron microscopy (blue lines). (C) Scanning electron micrograph for the tapered tip of the pulled capillary.

The explanation for this follows by considering a single cell, where the dynamics of the surrounding plasma are dominated by viscous forces (Reynolds number Re $< 10^{-3}$), and a lubrication-like formalism[21] describes its flow in the narrow, almost-parallel gap between the RBC and the tube wall. K_T can then be estimated by assuming that the cell, flowing at a velocity u, adopts a shape of radius $a = r - h$, where h is the characteristic small clearance between the cell and the capillary wall. The longitudinal driving pressure drop across the cell δ leads to a resultant force δr^2 which is balanced by the viscous force $\dfrac{\mu u r \ell}{h}$ on the capillary wall (see Fig. 1A). When combined with fluid continuity in the gap, expressed as $rh\bar{v} \sim r^2\bar{v} - a^2 u$ or equivalently $\dfrac{\bar{v}}{u} \sim 1 - \dfrac{h}{r}$, we find

$$K_T \sim \frac{r}{h}. \tag{1}$$

In the limit of a rigid cell, K_T will thus increase sharply when $r \to a$ (*i.e.*, $h \to 0$).

Realistically, below a critical radius r_c, confinement may impose areal stretching, or significant bulk deformations in an impaired cell, and the tension in the membrane, or other elastic response, couples to the flow to make K_T also dependent on $\bar{v}$. To date, experimental and theoretical studies on single RBC motion have reported a ten-fold increase in K_T, thus showing only a moderate role for RBC deformability relative to the driving pressure gradient. As confinement increases, the range of low velocity and/or the stiffening of the cell poses a challenge to both experiment and theory/computations[1] as K_T increases even more. This previously unstudied regime, where a single RBC can significantly obstruct the flow, is the subject of the present article.

To understand this pressure-driven occlusive flow of RBCs confined to a capillary when $2r \leq 7$ μm, here we describe an *in vitro* experimental study of the motion of a single deformed RBC and the suspending plasma flow that isolates the essential physical parameters controlling this process. We complement this with an elasto-hydrodynamic model that provides a minimal description of the phenomena.

II. Materials and methods

A. Flow device fabrication

To observe the pressure-driven motion of a single RBC, we custom-designed a novel flow device, shown in Fig. 1A, consisting of a tapered cylindrical capillary with an inner diameter $2 \leq 2r(z) \leq 580$ μm varying with the axial position z (see Fig. 1A). Cylindrical borosilicate capillaries (1B100-6, World Precision Instruments, Sarasota FL, USA) were first pulled using a pipette puller (P-97, Sutter Instrument, Novato CA, USA) with pulling and heating parameters that resulted in a capillary with a centimeter long tapered tip. This tapered capillary was further micro-forged to a desired minimum diameter of 2 μm.

The inner wall of the tapered borosilicate capillary was chemically treated to inhibit the adhesion of RBCs to the capillary wall during flow. The first stage in this treatment involved rendering the capillary inner walls hydrophobic through silanization. The wide-end of the capillary was connected to a syringe with stub needle using vinyl tubing and the syringe was drawn back to suck air in from the tapered tip. The tapered tip of the pipette was dipped in 5% dimethyldichlorosilane in hexane solution (silanization solution I, Sigma-Aldrich, St. Louis MO, USA) that was sucked into the capillary. The capillary was then allowed to dry for two minutes before being placed in an oven for overnight incubation at 100 °C. The incubation allowed the fixation of the silane coating to the capillary walls. Following incubation, the pipette was inserted through a hole drilled in the side wall of a Petri dish (60 × 15 mm, Becton Dickinson, Franklin Lakes NJ, USA) and sealed with fast acting epoxy. The Petri dish serves as the receiving discharge

reservoir as shown in Fig. 1A. The pipette was then immersed in a 0.5% surfactant Pluronic F-127 solution in 0.5× phosphate buffered saline (PBS) solution (PBS Cellgro, Mediatech, Manassas VA, USA). This triblock surfactant was adsorbed onto the hydrophobic silanized glass surface to create a nanometer-thick layer that inhibited biological adhesion.[22] In order to ensure that silane fixation to capillary walls had occurred satisfactorily, the meniscus of the surfactant–PBS solution was monitored under a microscope as it was drawn into the capillary under suction. Loose fixation of the silane coating resulted in one of the two possibilities. Either the meniscus of the surfactant–PBS solution was not flat thus implying the absence of a hydrophobic coating, or one observed fluctuations in the meniscus as the surfactant–PBS solution was carefully drawn up the tapered section, thereby implying spatially inhomogeneous fixation of silane to inner capillary walls. Devices that exhibited either feature were rendered defective, and were not used in the experiment.

The tapered glass capillary offers the ability to probe RBC confinement behavior continuously over a range of confinement radii, and the physiological similarity to the cylindrical geometry of real capillaries (in contrast to the rectangular channels in soft lithography) with smooth walls. Although glass capillaries are not deformable, by adjusting the distension of the RBC, we tuned the relative confinement and deformability to operate in a regime where the cell almost completely occludes flow.

B. Inner diameter measurements

Devices that passed both the chemical treatment stages of silanization and surfactant coating were then thoroughly washed with Pluronic-free PBS solution flow in the capillary, and mounted on an inverted microscope (Zeiss Axiovert 200, Jena, Germany). When filled with liquid only, the inner diameter of the capillary could be measured from bright field micrographs. The microscope was set to Köhler illumination in order to maximize the contrast of the inner wall, and micrographs of lateral views of the capillary were acquired at an on-screen magnification of 54 nm per pixel. The inner diameter measurements were obtained from image analysis algorithms developed in-house that extract the brightness weighted sub-pixel locations of the two central illumination peaks which correspond to the inner walls of the glass tube.[23] Understanding the light-transmission imaging of a hollow glass tube is a challenging ray-tracing problem. Notably, the obtained micrograph depends strongly on the position of the microscope's plane of focus relative to the capillary. In Fig. 1B, we show the variation of the brightness profile (horizontal grayscale lines) produced by the light transmitting through the glass tube, at its tip, for various levels of focus. In red are the locations of the brightness dark peaks, as extracted by our algorithm at each plane of focus. In blue are the true inner and outer diameters, as measured from the scanning electron microscopy image of the same capillary tip and shown in Fig. 1C. We thus observe that there is a plane of focus, where the tube's outer walls produce noticeably darker bands, and where the algorithm extracts an unbiased measure of the inner diameter. We also find that our image analysis algorithms could measure the inner

tube radius to within 1/2 pixel, that is about 25 nm. The inner radius was extracted at regular intervals along the tapered section to measure the variation $r(z)$ of the tube radius with the position z in the tapered tip. By construction, the pipette has smooth inner walls, and we find that $r(z)$ can be very effectively fitted to an exponential function over a tapered length of about 3 mm,[24] thus including more than 20 experimental points (see blue squares in Fig. 2A). Using this function to describe the true, smooth shape of the capillary allows us to improve the spatial resolution on $r(z)$ measurement, reducing it by 50%, to about 10 nm.

C. Loading the flow device with RBCs

A blood sample obtained from a healthy donor was diluted to 1.5% hematocrit, washed three times in 0.5× PBS solution, then immediately injected into the capillary, and further allowed to settle towards the tapered end *via* sedimentation. The flow device was then connected to a hydrostatic reservoir (also containing 0.5× PBS solution) mounted on a vertical linear translation stage for height control. When a single RBC reached the desired confinement, the reservoir was set to a defined height H above the discharge level, thus imposing a driving pressure head $\Delta = \rho_b g H$ ($\rho_b = 10^3$ kg m^{-3} is the density of the PBS solution and g is the gravity). We verified that controlled hydrostatic pressure head as low as 1 Pa could be applied (*i.e.* $H \sim 100$ μm).

The flow device was mounted back on the inverted microscope, to which a camera (PixeLINK, Ottawa, Canada) was attached to acquire movies of the cell motion at various frame rates. The movies were then analyzed using a custom tracking algorithm to extract the positions of the RBC in the tube with a resolution of 0.05 μm. We note that to be visible through the curved glass, the wall-cell gap h must be greater than about 300 nm.

III. Results

Before being injected into the flow device, the cells are pre-swollen in a hypotonic buffer and their new volume Ω_s can be estimated using Ponder's relation[14,25] $\Omega_s = \Omega_p \left(1 + R_w \dfrac{1 - c}{c} \right)$. Here $\Omega_p = 90 \pm 10$ μm^3 is the physiological volume of a cell,[14] $c = \dfrac{C}{C_p}$ is the relative osmolarity (or "tonicity") of the solvent (C and $C_p = 0.3$ mol L^{-1} being the buffer and physiological osmolarity, respectively), and $R_w = 0.57$ is the empirical volume fraction of so-called "active" water in the cell.[14]

Red cells have an unstretched membrane area $\Sigma_p = 135 \pm 10$ μm^2 under physiological conditions.[14] They become spherical for a buffer tonicity $c \approx 0.47$, an onset value obtained by substituting $\Omega_s = \dfrac{4\pi}{3} \left(\dfrac{\Sigma_p}{4\pi} \right)^{3/2}$ (volume of a sphere with surface area Σ_p) into Ponder's equation. For $c < 0.47$, the membrane is stretched, hence subject to tension, to allow further swelling. The Laplace pressure can then alter the osmotic balance to produce a slight departure from Ponder's relation, which thus

needs to be corrected accordingly as explained later. The experiments are performed with c slightly above 0.47, so that an unconfined preswollen RBC is only moderately inflated (yet spheroidal in shape) with a volume $\Omega_s < \frac{4\pi}{3}\left(\frac{\Sigma_p}{4\pi}\right)^{3/2}$ and a relaxed, tension-free membrane of area Σ_p. Such a preswollen spheroidal unconfined cell has a mean diameter of $\sim$6 µm and can be seen in the inset 1 of Fig. 2A. The other numbered micrographs on Fig. 2A show the characteristic shapes of the cell at various confinement levels. For a tube with inner diameter $2r < 6$ µm, the cell adopts a sphero-cylindrical shape (i.e. a cylinder capped by hemispheres). The rightmost image (micrograph 7), showing the low-contrast, gel-like cytoplasmic content of the cell, is described in Section IIIC.

In the first set of experiments, we followed the motion of isolated RBCs under constant pressure head $\Delta \geq 50$ Pa, and calculated their velocity $u(z)$ from their trajectory at various locations z in the tube; an example is shown in Fig. 2A and Movie S1 (ESI†). The range of velocities considered here is typical for blood flows in the capillaries of the human microcirculation.[26,27] It is then useful to compare u with the mean Poiseuille velocity of a blood-free, purely viscous PBS solution flowing in the same tapered tube and under the same pressure head. We call this blood-free plasma velocity $\bar{v}_\varnothing$ (v "empty") and it is calculated (see the Appendix) as

$$\bar{v}_\varnothing(z) = \frac{\gamma(z)r(z)\Delta}{8\mu}, \qquad (2)$$
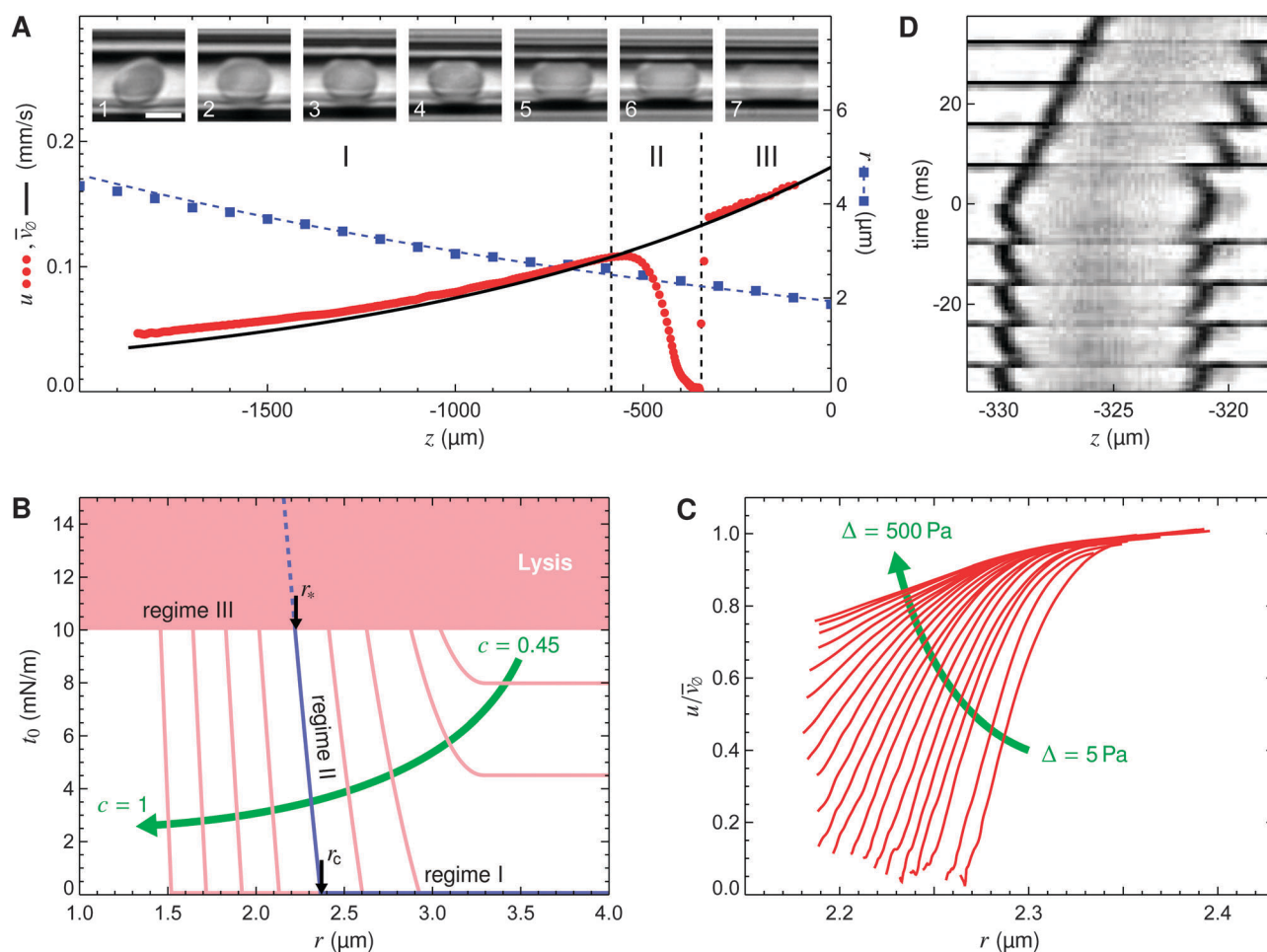

Fig. 2 (A) The three regimes of RBC flow in a capillary: (I) the RBC behaves as a tracer of the Poiseuille flow; (II) the confined RBC stretches into a spherocylindroid shape with a significantly lower velocity and almost stops; and (III) RBC lyses when the cell spills its cytoplasmic content which flow with a Poiseuille profile (see also Movie S1, ESI†). The circles (red) plot the RBC velocity in the three regimes, with the solid line (black) representing Poiseuille flow. The squares (blue) plot capillary radius vs. position in the tube, and the dotted line (blue) is an exponential fit. The numbered insets show the RBC confined at the corresponding locations in the tube (scale bar: 5 µm). (B) The tension in the membrane as a function of the confinement radius, for various values of osmolarity, as calculated using eqn (3) (red lines). The blue line is for $c = 0.55$, as observed in the experiments (see Section IV). The 3 regimes encountered in our experiments are indicated along the curve. After lysis, the tension vanishes in the ruptured membrane. (C) RBC velocity u, normalized by Poiseuille flow velocity $\bar{v}_\varnothing$ in the same but cell-free tube vs. confinement radius for various pressure heads Δ. (D) Video micrograph snapshots of the sphero-cylindroid shaped RBC before (bottom half) and after (top half) the lysis (time 0) showing the cell's retraction from the back (see also Movie S2, ESI†).

where $\gamma(z) = \left[r(z)^3 \int_{tube} r(\zeta)^{-4} d\zeta\right]^{-1}$ is the effective tube aspect ratio ($\gamma = \frac{r}{L}$ for a straight cylinder of radius r and length L). We can evaluate $\bar{v}_{\varnothing}(z)$ from knowing Δ, $\mu = 8.9 \times 10^{-4}$ Pa s and the measurements of $r(z)$.

Comparing $u(z)$ (red circles in Fig. 2A) with $\bar{v}_{\varnothing}(z)$ (black line in Fig. 2A) allows us to isolate three regimes in the dynamics of a single cell.

A. Regime I: cell as a passive flow tracer

In the first regime when $r(z) > r_c$ (for $z < -600$ µm in Fig. 2A), we observe that $u(z)$ is comparable to $\bar{v}_{\varnothing}(z)$ and the cell acts as a flow tracer, without significantly modifying the Poiseuille regime for the viscous plasma. For low confinement ($r(z) > 3$ µm, i.e. $z < -1400$ µm), $\bar{v}_{\varnothing}(z) < u(z) < 2\bar{v}_{\varnothing}(z)$, and the cell follows streamlines at the center of the tube, with a visible gap between the cell and tube walls (see inset micrographs 1 and 2 in Fig. 2A). At slightly higher confinement (for $-1300 < z < -600$ µm), $u(z) \sim \bar{v}_{\varnothing}(z)$, and the cell also follows the mean Poiseuille flow without causing resistance even though the clearance between the cell membrane and the tube walls is undetectable (see insets 4 and 5 in Fig. 2A).

Although it is difficult to measure the gap h directly, we can estimate a lower bound for h above which the flow remains unperturbed by the cell. To do so, we first note that the pressure drop created across the cell $\delta(z)$ is linked to the pressure head via the relation $\frac{\delta(z)}{\Delta} + \frac{\bar{v}(z)}{\bar{v}_{\varnothing}(z)} = 1$ (eqn (A.2) in the Appendix). Here $\bar{v}(z)$ is the average velocity of the plasma surrounding the cell, and $\bar{v}_{\varnothing}(z)$ has been defined earlier by eqn (2) as the mean Poiseuille velocity of the plasma in the cell-free tube. Hence the cell is a non-invasive tracer, i.e. $u \sim \bar{v} \sim \bar{v}_{\varnothing}$, as long as $\frac{\delta}{\Delta} \ll \frac{\bar{v}}{\bar{v}_{\varnothing}}$. The latter inequality can equivalently be written as the geometric criterion $h \gg \frac{\gamma \ell}{4}$ after substituting $\bar{v}_{\varnothing} = \frac{\gamma r \Delta}{8\mu}$ (eqn (2)) and the relation $\delta = \frac{2\mu \bar{v} \ell}{rh}$ derived for a flowing sphero-cylindrical object of length ℓ (eqn (A.19) in the Appendix; in the regime described here, the cell can accommodate the confined flow without stretching its membrane). From the measurement of $r(z)$ (Fig. 2A), we typically extract $\gamma \approx 10^{-2}$ at a diameter $2r \approx 5$ µm where $\ell \approx 4$ µm. We thus obtain $\frac{\gamma \ell}{4} \approx 10$ nm for the lower bound of h above which the tracer regime is still observed. Note that this value is remarkably low compared to the tube radius. In the range $10 \ll h < 300$ nm, the cell will not significantly disturb the plasma flow even if there is no visible clearance between the RBC and the capillary inner walls. This finding is indeed consistent with our observations of inset micrographs 4 and 5 in Fig. 2A, but also with the values of h reported later in the text for the occlusive regime (Fig. 3A).

B. Regime II: flow occlusion by a soft confined cell

As the cell moves further towards smaller tube radii, it exhibits a different dynamic regime and slows down significantly. The increase in the membrane area of the cell due to confinement in the capillary tube leads to an isotropic uniform tension t_0 in the membrane that stiffens the cell and resists the flow, when the radius falls below $r = r_c$. At this point, the cell adopts a sphero-cylindrical shape of volume Ω_s, radius r_c, and area Σ_p that are related by the geometry via $\Sigma_p = \frac{2\Omega_s}{r_c} + \frac{4\pi r_c^2}{3}$. This relation can be used to solve for r_c as a function of Ω_s, hence as a function of c. For radius $r < r_c$, the membrane must stretch to an area $\Sigma > \Sigma_p$ and a tension $t_0 = K\frac{\Sigma - \Sigma_p}{\Sigma_p}$ arises, with $K = 450$ mN m^{-1} being the elastic area stiffness of the RBC membrane.[28–30] Concurrently the volume of the cell decreases to $\Omega < \Omega_s$, because the osmotic pressure balance is offset by the Laplace term $\frac{2t_0}{r}$ produced by the tense membrane.[31] Under the assumptions of Evans and Waugh,[31] one may evaluate the corrected volume $\Omega = \Omega_s\left(1 - \frac{2t_0}{\Pi cr}\right)$, with $\Pi = \frac{RTC_b}{R_w} = 1.3 \times 10^6$ Pa the physiological osmotic pressure at temperature $T = 25$ °C (R being the ideal gas constant).

Combining Ponder's relation, its osmotic correction for a tense membrane and the geometric condition of the spherocylinder $\Sigma = \frac{2\Omega}{r} + \frac{4\pi r^2}{3}$, we can finally express the tension t_0 in terms of r, Σ_p, Ω_p and c as the solution of the equation:

$$\frac{t_0}{K} + 1 = \frac{2\Omega_p}{r\Sigma_p}\left(1 + R_w\frac{1-c}{c}\right)\left(1 - \frac{2t_0}{\Pi cr}\right) + \frac{4\pi r^2}{3\Sigma_p}. \tag{3}$$

In Fig. 2B we plot our predictions for tension t_0 in the membrane as a function of the confining radius r. As r decreases, the tension sharply increases from 0 when $r < r_c$. For $c < 0.47$, a preswollen cell exhibits a tense membrane even if it is not confined, as shown in Fig. 2B by the nonzero constant tension curve at large r in this case.

Increasing the membrane tension at constant osmolarity implies an increase in the force driving the cell to greater confinement. In other words, membrane tension produces a stress resisting the flow of the confined cell and eventually induces the occlusion. In our case $c > 0.47$, and setting $t_0 = 0$ in eqn (3) allows us to solve for the critical radius r_c associated with the transition to $t_0 > 0$ and occlusive flow. This yields $r_c = 2.4$ µm for $c = 0.55$ (see Section IV for this choice of c). However natural variations in Ω_p and/or Σ_p (of the order of 5%) produce significant changes in the estimation of r_c, in agreement with our observations that different cells do not consistently enter the occlusive regime at the same location (thus discarding any role of wall defects) for a given tube.

For reproducibility, we used the same cell to focus on this regime where tension competes with lubrication. In a second set of experiments, we thus used an oscillatory pressure head Δ to first locate r_c for the cell and then span the dynamics of the occlusive regime when the radius is in the range $r_* < r < r_c$ (r_* marks the next regime, see below) and the pressure head $5 < \Delta < 500$ Pa. In Fig. 2C, we show the scaled speed of the cell $u/\bar{v}_{\varnothing}$ as a function of confinement radius; as the pressure head

is increased, the relative velocity of the cell changes by more than an order of magnitude in this occlusive zone.

We will discuss this regime in more detail in Section IV.

C. Regime III: cell lysis and flow recovery

When confinement produces tension greater than about 10 mN m^{-1} (an area increase of about 2%)[28] that corresponds to a tube radius $r_* \approx 2.2$ μm (solving eqn (3) with $t_0 = 10$ mN m^{-1}), the cell finally lyses. In this third regime, there is a sharp rise in the velocity of the cell, and observations show that at this transition, the cell first retracts from the back by a few percent (Fig. 2D and Movie S2, ESI†), consistent with the estimated stretch ratio required to rupture the membrane. Indeed, the tracked object in this regime appears to be the gel-like cytoplasmic content of the cell released after lysis (see the rightmost inset of Fig. 2A), which follows the flow as a passive tracer (see regime III data for Fig. 2A). The ability to further observe the ruptured post-lysis membrane sack flowing (not shown here) strongly suggests that RBC arrest is due to physical blockage, not physico-chemical adhesion.

IV. Discussion

The dominating forces occurring in the confined regime II detailed above (Section IIIB) are found in the clearance between the cell membrane and the tube wall. To investigate the elasto-hydrodynamic balance in this regime, it is then judicious to extract the local measurement of lubrication gap height h. Yet, as pointed out earlier, our optics does not allow the direct measurement of clearance h. We adopt here an indirect approach, where we extract h from the measurements of u and r presented in Fig. 2. To do so, we use the three hydrodynamic relations given below:

$$1 = \frac{\delta(z)}{\Delta} + \frac{\bar{v}(z)}{\bar{v}_\varnothing(z)}, \tag{4a}$$

$$\frac{\bar{v}}{u} = 1 - f_1\left(\frac{\ell}{\sqrt{2rh}}\right)\frac{h}{r}, \tag{4b}$$

$$\delta = f_2\left(\frac{\ell}{\sqrt{2rh}}\right)\frac{2\mu u \ell}{rh}, \tag{4c}$$

where $f_1(\alpha) = 1 + \frac{\pi}{3\pi + 8\alpha}$ and $f_2(\alpha) = f_1(\alpha) + \frac{2\pi}{\alpha}$. The derivation of these three relations is shown in the Appendix, and they express, respectively, the continuity of pressure, the incompressibility of the plasma, and the hydrodynamic force balance. They are thus based on purely hydrodynamical considerations, without assuming an elastic model for the cell, although the confined cell shape is approximated by a sphero-cylinder in order to obtain the functionals f_1 and f_2. In the three independent equations, only δ, $\bar{v}$ and h are the non-measurable, unknown parameters. We can thus solve for all 3 unknown parameters, using the measured remaining input, to obtain an indirect, yet experimental, measurement of lubrication clearance height h as a function of u and r. The value obtained for h is, by construction of the model, the one for which the cell is better approximated by a sphero-cylinder of radius $a = r - h$.

We show in Fig. 3A our results regarding h *vs.* u with the different lines representing different radii $2.2 < r < 2.3$ μm for the same single RBC. The values of h are in the nanometer range, which illustrates the sensitivity of our methods, owing to the low effective aspect ratio of the tube used here (see also Section IIIA). We note that the Debye length in the plasma buffer is about[32] 1 nm. The amplitude of membrane thermal fluctuations, estimated at $T = 25$ °C by $\left(\frac{k_B T}{t_0}\right)^{1/2}$ (k_B being the Boltzmann constant) is also about 1 nm at most, for the $\sim$mN m^{-1} tensions encountered here. Hence electrostatic and thermal effects may challenge our hydrodynamic interpretation at this length scale, and we did not report any value of h below 1 nm. Well above this threshold, the curves show a transition between two power-law regimes that we discuss now.

Calculating the scaled gap $\varepsilon = \frac{h}{r}$ and the capillary number $\text{Ca} = \frac{\mu u}{t_0}$, with the tension obtained from eqn (3), allows us to show the variation of $\frac{r^2}{\ell^2}\varepsilon$ as a function of $\frac{r^3}{\ell^3}\text{Ca}$ in Fig. 3B. We see that the experimental data follow a single master curve, with the cell area Σ_p, volume Ω_p and plasma osmolarity c chosen to maximize data collapse: $\Sigma_p = 132.3$ μm^2, $\Omega_p = 85.5$ μm^3 and $c = 0.55$. The osmolarity is a fitting parameter to account for residual solutes not washed away from the blood sample. In this case, we note that the tension t_0 is found between 1 and 5 mN m^{-1}, well above the value $|\tau|$ of its characteristic variation in the membrane, estimated with eqn (A.15) to be at most 0.1 mN m^{-1}. This observation justifies the approximation of uniform tension $t_0 \gg \tau$ used in the Appendix (Section 5) to derive the elasto-hydrodynamic scalings we use below. Furthermore, these values of t_0 are above an eventual uncertainty $\sim$0.5 mN m^{-1} that may originate from the limited spatial resolution when measuring the radius r.

We repeated this procedure for a cell in plasma with higher osmolarity, 0.6× PBS, and reported in blue in Fig. 3B the average curve obtained at the best data collapse, this time for $\Sigma_p = 135.5$ μm^2, $\Omega_p = 85$ μm^3 and $c = 0.64$, but at confinement radii between 1.8 μm and 1.9 μm. The rightmost part of this blue curve is subject to high uncertainty, because the calculated tension in this part of the curve is about 0.5 mN m^{-1} or less, close to its standard deviation. These small values are also comparable to the characteristic variation $|\tau|$ of tension in the membrane, in which case the elasto-hydrodynamic scalings derived in Section 5 of the Appendix may not be valid anymore. The occlusive regime with a tense membrane occurs when the cell is already significantly elongated in that case. Nevertheless, the leftmost part of the blue curve, where membrane surface tension is above 1 mN m^{-1}, coincides with the red curve obtained at lower osmolarity.

Disregarding the small deviation of the blue curve from the master curve, we can extract the following scalings from Fig. 3B (dashed lines):

$$\varepsilon = \begin{cases} (7 \pm 3) \times \left(\frac{\ell}{r}\right)^{-0.10 \pm 0.10} \text{Ca}^{0.70 \pm 0.03} & \text{for } \ell > \ell_c, \\[2mm] (0.04 \pm 0.01) \times \left(\frac{\ell}{r}\right)^{1.04 \pm 0.06} \text{Ca}^{0.32 \pm 0.02} & \text{for } \ell < \ell_c, \end{cases} \tag{5}$$
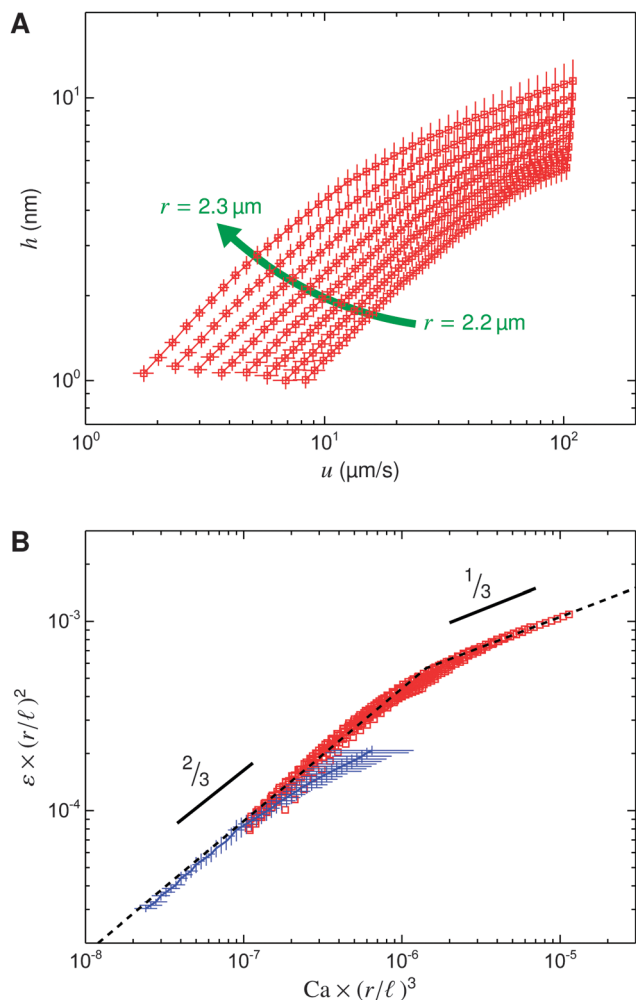
Fig. 3 (A) Lubrication gap size h between the cell and capillary walls plotted against the cell velocity u for several tube radii 2.2 μm < r < 2.3 μm. (B) Scaled lubrication gap size $\frac{h}{r}\left(\frac{r}{\ell}\right)^2$ between the cell and capillary walls plotted against the scaled cell velocity $\frac{\mu u}{t_0}\left(\frac{r}{\ell}\right)^3$ for 2.2 μm < r < 2.3 μm showing a characteristic change in power law scaling from $\varepsilon \sim Ca^{2/3}$ for small velocity to $\varepsilon \sim Ca^{1/3}$. The red curve is from the data shown in (A), while the blue line is from a separate experiment.

with $\ell_c \approx 30\sqrt{2hr}$. These scalings are thus in agreement with our simple elasto-hydrodynamic model derived in the Appendix, eqn (A.25), and the measured length ℓ_c that marks the transition from a long cylindrical cell to a short spherical cell is also in fair agreement with our hydrodynamic calculation (Fig. 4 in the Appendix). We could only investigate a fraction of decade of the 1/3 power law regime and cannot confidently assess whether this regime is maintained for higher velocities. Some studies suggest an oscillatory behavior of the clearance size as a function of the length of the confined cell,[33,34] which may indeed make the 1/3 power law regime spanning less than a decade.

We finally note that the numerical solution of the Landau–Levich equation in the case of an infinitely long cell or bubble, treated by Bretherton[35] and Secomb et al.,[9] gives the prefactor to the scaling $\varepsilon = 2.123 \times Ca^{2/3}$. Although our measurement is consistent with this order of magnitude, the moderate discrepancy may come from finite-length effects or the oversimplified sphero-cylinder geometry assumed for the cell.

V. Conclusions

We have reported here the measurements of the motion of a single RBC in a tube with various levels of confinement and driving pressure head. We have shown that there is a range of confinement radii where the cell significantly alters the flow to almost arrest it. In this regime, we were able to extract precise values of lubrication clearance height h from a purely hydrodynamic interpretation of our measurement. We have explained this regime with a simple elasto-hydrodynamic model which predicts the dependency of lubrication clearance height h between the tube wall and the cell. We observed that the gap height increases for increasing velocity and decreasing confinement, following a power-law that depends on the length of the confined cell. By using the estimate eqn (1), $K_T \sim \frac{r}{h} = \varepsilon^{-1}$, we note that the values observed for h correspond to an intrinsic viscosity $200 \leq K_T \leq 2000$, a range that is directly relevant to the study of flow occlusion more broadly. In this regime the apparent viscosity μ_a will follow a power law dependency with the cell velocity and the tube radius according to eqn (5).

Our study highlights the role of lateral confinement in the increase in the effective viscosity of an RBC that strongly occludes flow, and thus paves the way for the study of vaso-occlusion in a variety of pathophysiological conditions associated with restricted blood flow in instances such as sickle cell disease, malaria, clots etc. But it may also appear relevant for physiological filtration processes relying on highly confined flow, e.g. in splenic sinuses.[36] More generally, it shows how pressure-driven flow of soft objects couples to confinement[37] and sets the stage for adhesion to the wall[38] to ultimately arrest motion and eventually cascade to larger scales to form a jam or clot.

Appendix

The occlusion originates from the elasto-hydrodynamic balance between the hydrodynamic forces, pushing the cell membrane away from the tube wall to maintain the lubrication layer of the liquid, and the tension in the membrane that resists confinement. This force balance occurs in the lubrication layer itself, and we need a local measurement of its height h to access the elasto-hydrodynamic balance. In this appendix, we derive from lubrication theory a set of equations that permit us the access h from the measurements obtained in regime II and summarized in Fig. 2C. The last section gives a scaling analysis of the elasto-hydrodynamic force balance.

1. Macroscopic flow

We consider the RBC confined and traveling in a slowly-tapered capillary of radius $r(z)$, filled with a liquid, or plasma, of viscosity μ. At the wider extremity of the capillary $z = z_0$, a pressure $P(z = z_0) = \Delta$ is applied, and the pressure at the other tapered edge of the

capillary is imposed at $P(z = z_0 + L) = 0$. The incompressible liquid then flows with an average flow rate $q = \pi\bar{v}(z)r(z)^2$ (in the direction of increasing z, see Fig. 2 of the main text), where $\bar{v}(z)$ is the average flow velocity at position z, and the RBC moves at a velocity $u(z)$ ($\bar{v},u \geq 0$ for $\Delta \geq 0$). Far from the cell, the pressure field P and the liquid velocity field V are determined by the lubrication approximation in the tapered tube ($r'(z) \ll 1$). We thus have

$$V(\rho,z) \overset{\text{far from}}{\underset{\text{the cell}}{=}} v_0(\rho,z) = \frac{2q}{\pi r(z)^2}\left[1 - \frac{\rho^2}{r(z)^2}\right], \quad (A.1a)$$

$$P(z) \overset{\text{far from}}{\underset{\text{the cell}}{=}} p_0(z) = \frac{8\mu q}{\pi}\int_z^{z_0+L} r(\zeta)^{-4}\mathrm{d}\zeta, \quad (A.1b)$$

which define the fields $v_0(\rho, z)$ and $p_0(z)$, where ρ is the radial distance from the center of the tube.

Plugging the boundary condition $P(z_0) = \Delta$ into eqn (A.1b) uniquely gives the flow rate: in the absence of the cell in the tube, this yields $q_\varnothing = \pi\bar{v}_\varnothing(z)r(z)^2 = \frac{\pi\Delta}{8\mu}\left[\int_{z_0}^{z_0+L} r(\zeta)^{-4}\mathrm{d}\zeta\right]^{-1}$, *i.e.* eqn (2) used in the main text. If the RBC is in the tube at a position z, then the condition $P(z_0) = \Delta$ becomes

$$\Delta = \frac{8\mu q}{\pi}\int_{z_0}^{z_0+L} r(\zeta)^{-4}\mathrm{d}\zeta - \int_{\text{gap}}[P'(\zeta) - p_0'(\zeta)]\mathrm{d}\zeta,$$

that we write as

$$\frac{\delta(z)}{\Delta} = 1 - \frac{q}{q_\varnothing} = 1 - \frac{\bar{v}(z)}{\bar{v}_\varnothing(z)}, \quad (A.2)$$

where $\delta(z) = -\int_{\text{gap}}[P'(\zeta) - p_0'(\zeta)]\mathrm{d}\zeta$ is the additional pressure jump associated with the RBC, with the integral evaluated over the length of the gap between the cell membrane and the tube wall, and with $P - p_0$ being non-zero only in this gap with clearance much smaller than the tube radius $r(z)$.

When N cells are flowing in file in the tube, eqn (A.2) becomes $\frac{N\delta}{\Delta} = 1 - \frac{8\mu\bar{v}L}{\Delta r^2}$ if the capillary is a straight cylinder of radius r and length L. The tube hematocrit is defined as $H_T = \frac{N\Omega}{\pi r^2 L}$ with Ω the volume of each cell. The apparent viscosity is given by Poiseuille's law $\mu_a = \frac{\Delta r^2}{8\bar{v}L}$ and yields the effective viscosity of a Newtonian fluid that would flow in the capillary tube at the same velocity $\bar{v}$ under load Δ. We may thus write eqn (A.2) as $\mu_a = \mu(1 + K_T H_T)$ with $K_T = \frac{1}{8}\frac{\pi r^2\ell}{\Omega}\frac{1}{\mu}\frac{\delta r^2}{\bar{v}\ell}$ for a cell of length ℓ. Since $\Omega \sim \pi r^2\ell$ for a confined cell, we obtain $K_T \sim \frac{1}{\mu}\frac{\delta r^2}{\bar{v}\ell}$.

2. Lubrication hydrodynamics in the cell-wall clearance

To gain more insight, we can approximate the pressure profile in the gap between the RBC and the tube wall using a lubrication theory.[35] Here $v(\rho,z) = V(\rho,z) - v_0(\rho,z)$ and $p(z) = P(z) - p_0(z)$. We will write the dependency of various quantities on z only

if they vary significantly over the axial length of the gap. Hence,

$$r(z) = r, \; u(z) = u, \; \bar{v}(z) = \bar{v}, \; p_0(z) = p_0, \; \delta(z) = \delta,$$

while we explicitly write, for example, $p(z)$ and $v(\rho,z)$.

In the gap between the cell and the tube wall, we write the lubrication equation:

$$p'(z) = \mu\frac{1}{\rho}\frac{\partial}{\partial\rho}\left[\rho\frac{\partial v(\rho,z)}{\partial\rho}\right], \quad (A.3)$$

while the liquid incompressibility is expressed in terms of flow rates:

$$q = u\pi a(z)^2 + 2\pi\int_{a(z)}^r V(\rho,z)\rho\,\mathrm{d}\rho$$

$$= u\pi a(z)^2 + q\left[1 - \frac{a(z)^2}{r^2}\right]^2 + 2\pi\int_{a(z)}^r v(\rho,z)\rho\,\mathrm{d}\rho, \quad (A.4)$$

where we have used the expression of $v_0(\rho, z)$ given by eqn (A.1a), and where $a(z)$ describes the profile of the cell radius. The boundary conditions for the liquid velocity are:

$$v(r,z) = 0, \quad (A.5a)$$

$$v(a(z),z) = u - v_0(a(z),z). \quad (A.5b)$$

Solving the system of eqn (A.3)–(A.5) for $p'(z)$ gives, keeping only the leading order terms,

$$-\frac{r^2}{6\mu u}p'(z) = (\chi - 1)\frac{r^3}{h(z)^3} + \frac{\chi+1}{2}\frac{r^2}{h(z)^2} + \frac{7\chi+3}{30}\frac{r}{h(z)} + \cdots \quad (A.6)$$

where $\chi = \bar{v}/u$ is the capillary hematocrit ratio[9,39] and $h(z) = r - a(z) \ll r$ is the gap. One can also calculate the scaled viscous stress at the tube wall,

$$\frac{r}{3\mu u}\left(-\mu\frac{\partial v}{\partial\rho}\bigg|_{\rho=r}\right) = (\chi - 1)\frac{r^2}{h(z)^2} + \frac{\chi+3}{3}\frac{r}{h(z)} + \cdots \quad (A.7)$$

and at the cell wall,

$$\frac{r}{3\mu u}\left(\mu\frac{\partial v}{\partial\rho}\bigg|_{\rho=a(z)}\right) = (\chi - 1)\frac{r^2}{h(z)^2} + \frac{2\chi}{3}\frac{r}{h(z)} + \cdots = -\frac{r}{3\mu u}t'(z), \quad (A.8)$$

the latter being balanced by the gradient of the tension $t'(z)$ in the membrane of the RBC.

Now defining the lengths

$$\ell_n = \int_{\text{gap}}\left[\frac{\varepsilon r}{h(z)}\right]^n\mathrm{d}z \quad \text{for } n = 1, 2\ldots, \quad (A.9)$$

where $\varepsilon \ll 1$ is the characteristic scaled size of the gap, we can express the additional pressure jump $\delta = -\int_{\text{gap}}p'(z)\mathrm{d}z$, the viscous force along the tube wall $\sigma = -\int_{\text{gap}}\mu\frac{\partial v}{\partial\rho}\bigg|_{\rho=r}\mathrm{d}z$, and the membrane tension jump $\tau = -\int_{\text{gap}}t'(z)\mathrm{d}z$ by integrating

Table 1 All notations used in the article

$a(z), a$	Radius of the cell[a]		P_i	Uniform pressure inside the cell
α	Scaled length of the cell's tubular region $\alpha = \ell/(2hr)^{1/2}$		Π	Osmotic physiological pressure at $T = 25\ °C$
α_c	Critical value of α for the cell's dynamic transition		q	Plasma flow rate
c	Scaled osmolarity $c = C/C_p$		$q_\varnothing$	Plasma flow rate in a cell-free tube
C	Osmolarity		$r(z), r$	Tube inner radius[a]
C_p	Physiological osmolarity		R	Ideal gas constant
Ca	Capillary number Ca $= \mu u/t_0$		Re	Reynolds number Re $= \rho_b r \bar{v}/\mu$
$\delta(z), \delta$	Pressure drop across the cell[a]		r_c	Onset radius of cell confinement
Δ	Hydrostatic pressure head		$r_\star$	Onset radius of cell lysis
ε	Scaled height of the lubrication clearance $\varepsilon = h/r$		R_w	Volume fraction of "active" water
$f_1(\alpha)$	Kinematic function for transition from the short to long cell		ρ	Radial cylindrical coordinate
$f_2(\alpha)$	Dynamic function for transition from the short to long cell		ρ_b	Mass density of buffer PBS
$\phi(x)$	Scaled excess pressure $\phi = p/(t_0/r)$		σ	Integrated viscous stress at the tube wall
g	Gravity		Σ	Surface area of the cell membrane in confinement
$\gamma(z), \gamma$	Effective tapered tube aspect ratio[a]		Σ_p	Physiological surface area of the cell membrane
$\Gamma(n)$	Euler gamma function of order n		$t(z), t$	Excess tension in the cell membrane[a]
$h(z), h$	Lubrication gap profile[a] $h = r - a$		T	Temperature
H	Hydrostatic reservoir altitude above discharge		$t_0(z), t_0$	Uniform isotropic tension in the cell membrane[a]
H_T	Tube hematocrit		τ	Tension drop in cell membrane across its length
η	Characteristic variation of h		$u(z), u$	Velocity of the cell[a]
K	Elastic area stiffness of the RBC membrane		$\bar{v}(z), \bar{v}$	Mean velocity of the plasma[a]
k_B	Boltzmann constant		$\bar{v}_\varnothing(z), \bar{v}_\varnothing$	Mean velocity of the plasma in a cell-free tube[a]
K_T	Intrinsic viscosity at the single cell level		$v(\rho,z)$	Excess plasma velocity field in the lubrication gap
ℓ	Length of the tubular region of the confined cell		$V(\rho,z)$	Plasma velocity field $V = v + v_0$
ℓ_c	Critical value of ℓ for the cell's dynamic transition		$v_0(\rho,z)$	Plasma velocity field far from the cell
ℓ_n	Lubrication gap length of order n (eqn (A.9))		Ω	Volume of the swollen cell in confinement
L	Length of the capillary tube		Ω_p	Physiological volume of the cell
λ	Characteristic axial length over which h varies by η		Ω_s	Volume of the unconfined osmotically swollen cell
μ	Plasma (PBS in our experiments) viscosity		x	Scaled axial cylindrical coordinate $x = (6Ca)^{2/3}z/(\varepsilon r)$
μ_a	Apparent blood viscosity		χ	Hematocrit ratio $\chi = \bar{v}/u$
n	Integer for the order number		$y(x)$	Scaled lubrication gap profile $y = h/(\varepsilon r)$
N	Number of cells in the capillary segment		$y_0(x)$	Scaled sphero-cylindrical gap profile (eqn (A.18))
$p(z), p$	Excess pressure field in the lubrication layer[a]		z	Axial cylindrical coordinate
$P(z)$	Pressure field $P = p + p_0$		z_0	z-Coordinate of the wider end of the capillary
$p_0(z), p_0$	Pressure field far from the cell[a]			

[a] The lack of explicit z-dependency in the notations indicates the characteristic magnitude of the corresponding z-dependent quantity; for example, b indicates a characteristic representative value for $b(z)$.

eqn (A.6), (A.7) and (A.8) respectively, to obtain

$$\frac{r^2}{6\mu u}\delta = \frac{\chi - 1}{\varepsilon^3}\ell_3 + \frac{\chi + 1}{2\varepsilon^2}\ell_2 + \frac{7\chi + 3}{30\varepsilon}\ell_1 + \cdots, \qquad (A.10a)$$

$$\frac{r}{3\mu u}\sigma = \frac{\chi - 1}{\varepsilon^2}\ell_2 + \frac{\chi + 3}{3\varepsilon}\ell_1 + \cdots, \qquad (A.10b)$$

$$\frac{r}{3\mu u}\tau = \frac{\chi - 1}{\varepsilon^2}\ell_2 + \frac{2\chi}{3\varepsilon}\ell_1 + \cdots \qquad (A.10c)$$

Longitudinal force balance on the cell yields the equation $\pi r^2 \delta = 2\pi r \sigma$. Using eqn (A.10a) and (A.10b) in this force balance allows us to solve for the capillary hematocrit ratio χ, and thus obtain the following expressions for δ and τ:

$$\chi = 1 - \frac{\ell_2}{\ell_3}\varepsilon + \left(\frac{\ell_1}{\ell_3} - \frac{\ell_2{}^2}{2\ell_3{}^2}\right)\varepsilon^2 + \cdots, \qquad (A.11a)$$

$$\frac{r^2}{6\mu u}\delta = \left(\frac{4\ell_1}{3} - \frac{\ell_2{}^2}{\ell_3}\right)\frac{1}{\varepsilon} + \cdots, \qquad (A.11b)$$

$$\frac{r}{6\mu u}\tau = \left(\frac{\ell_1}{3} - \frac{\ell_2{}^2}{2\ell_3}\right)\frac{1}{\varepsilon} + \cdots. \qquad (A.11c)$$

Using eqn (A.11a) into eqn (A.6), one finally writes the scaled pressure gradient, to leading order, as

$$-\frac{r^2}{6\mu u}p'(z) = \frac{r^2}{h(z)^2} - \frac{\ell_2}{\ell_3}\frac{r^3}{h(z)^3}\varepsilon + \cdots, \qquad (A.12)$$

which is the Reynolds equation.

3. Modified Landau–Levich equation

The normal force balance on the cell membrane in the lubrication gap is written as

$$[t_0 + t(z)]\left[\frac{1}{r} + h''(z)\right] = P_i - [p_0 + p(z)], \qquad (A.13)$$

where t_0 is the membrane tension at the front of the cell and P_i is the uniform pressure inside the cell, assuming that there is no flow inside the RBC. At the front of the cell (higher z), $(p,t) = (0,0)$ and at the back, $(p,t) = (\delta,\tau)$.

In our experiments the end caps of the confined RBC are hemispherical with radius r (see the inset of Fig. 2A), so that the normal stress balance, eqn (A.13), at the front and back of the

cell is written as

$$\frac{2t_0}{r} = P_i - p_0, \tag{A.14a}$$

$$\frac{2(t_0 + \tau)}{r} = P_i - (p_0 + \delta), \tag{A.14b}$$

respectively. From these relations, we can notably infer

$$-\frac{2\tau}{r} = \delta. \tag{A.15}$$

Assuming that the tension is uniform, high and equal to $t_0 \gg \tau$ in the RBC membrane, defining the capillary number $\text{Ca} = \frac{\mu u}{t_0}$, the scaled pressure $\phi = \frac{p}{t_0/r}$, the scaled gap $y(z) = \frac{h(z)}{\varepsilon r}$ and $x = \frac{(6\text{Ca})^{1/3}}{\varepsilon r} z$, eqn (A.12) and (A.13) now read

$$-\phi'(x) = \frac{(6\text{Ca})^{2/3}}{\varepsilon}\left[\frac{1}{y(x)^2} - \frac{\ell_2}{\ell_3}\frac{1}{y(x)^3}\right], \tag{A.16a}$$

$$\phi(x) = 1 - \frac{(6\text{Ca})^{2/3}}{\varepsilon} y''(x), \tag{A.16b}$$

where $\ell_n = \frac{\varepsilon r}{(6\text{Ca})^{1/3}}\int_{\text{gap}} y(x)^{-n}\mathrm{d}x$.

Contrasting the case studied here for a membrane, we note that for a bubble moving in a tube, the condition of vanishing tangential stress at the air–liquid interface, *i.e.* $\left.\frac{\partial v}{\partial \rho}\right|_{\rho=a(z)} = 0$, replaces the condition of eqn (A.5b) (while all other equations remain). In that case, eqn (A.16) are recovered, but the prefactor for Ca is 3 instead of 6 in both equations and in the definitions of x and ℓ_n.

The profile of the cell is obtained by eliminating ϕ in the system of eqn (A.16), which yields

$$y''' = \frac{1}{y^2} - \frac{\int y^{-2}}{\int y^{-3}}\frac{1}{y^3}. \tag{A.17}$$

Again, it is useful to contrast this result with that for a long bubble where the relation found by Bretherton is $y''' = \frac{1}{y^2} - \frac{1}{y^3}$, the Landau–Levich equation.[35] We can recover this limit (long cells) from eqn (A.17), which should otherwise be used for a finite-length bubble or membraneous cell, as is the case here.

4. Sphero-cylinder approximation

The modified Landau–Levich differential equation, eqn (A.17) is challenging to solve. As a first approximation, the shape of the confined RBC may be well described by a cylinder of length ℓ and radius $r(1 - \varepsilon)$, with hemispherical end caps, in which case $y(z) = y_0(z)$ given by

$$y_0(z) = 1 + \begin{cases} \dfrac{(z+\ell/2)^2}{2\varepsilon r^2} & \text{for } z < -\ell/2, \\[2mm] 0 & \text{for } |z| \leq \ell/2, \\[2mm] \dfrac{(z-\ell/2)^2}{2\varepsilon r^2} & \text{for } z > \ell/2, \end{cases} \tag{A.18}$$

where we use a quadratic approximation for the spherical ends, and we chose $z = 0$ at the center of the cell. Then we calculate $\ell_n = \ell + \frac{\sqrt{\pi}\Gamma(n - 1/2)}{\Gamma(n)}(2\varepsilon)^{1/2}r$, where Γ is the Gamma function, and eqn (A.11) yield

$$\chi = 1 - \varepsilon + \cdots, \tag{A.19a}$$

$$\frac{r}{\mu u}\delta = \frac{2\ell/r}{\varepsilon} + \cdots, \tag{A.19b}$$

$$\frac{1}{\mu u}\tau = -\frac{\ell/r}{\varepsilon} + \cdots \tag{A.19c}$$

We note that, in leading order, the last two equations agree with eqn (A.15), independently derived from the normal stress balance, and we thus validate the sphero-cylindrical approximation used here.

If the object is better approximated by a sphere, for which $\ell = 0$ and $\varepsilon = \min(h/r)$, then $\ell_n = \frac{\sqrt{\pi}\Gamma(n - 1/2)}{\Gamma(n)}(2\varepsilon)^{1/2}r$ and we find from eqn (A.11)

$$\chi = 1 - \frac{4}{3}\varepsilon + \cdots, \tag{A.20a}$$

$$\frac{r}{\mu u}\delta = \frac{8\pi}{(2\varepsilon)^{1/2}} + \cdots, \tag{A.20b}$$

in agreement with previous studies.[40,41] It is useful to understand the transition between these shapes, and to make this transparent, we introduce the scaled cell length $\alpha = \frac{\ell}{(2\varepsilon)^{1/2}r} = \frac{\ell}{(2hr)^{1/2}}$. Then $\frac{\ell_n}{(2\varepsilon)^{1/2}r} = \alpha + \frac{\sqrt{\pi}\Gamma(n - 1/2)}{\Gamma(n)}$, and we find the relations

$$\chi = 1 - f_1(\alpha)\varepsilon + \cdots, \tag{A.21a}$$

$$\frac{r}{\mu u}\delta = f_2(\alpha)\frac{4\alpha}{(2\varepsilon)^{1/2}} + \cdots, \tag{A.21b}$$

with

$$f_1(\alpha) = 1 + \frac{\pi}{3\pi + 8\alpha}, \tag{A.22a}$$

$$f_2(\alpha) = 1 + \frac{\pi}{3\pi + 8\alpha} + \frac{2\pi}{\alpha}, \tag{A.22b}$$

which allow us to interpolate between the two limits: setting $\alpha \gg 1$ leads to results pertinent to the cylinder (eqn (A.19)), while setting $\alpha \ll 1$ leads to results pertinent to the sphere (eqn (A.20)). In Fig. 4 we show a plot of function $f_2(\alpha)$, which is the prefactor characterizing the shape-dependent dynamics of the cell in eqn (A.21b). We notably see that the transition from a short cell (sphere regime) to a long cell (sphero-cylinder regime) occurs for $\alpha_c = \frac{\ell_c}{(2hr)^{1/2}} \sim 10$.

5. Elasto-hydrodynamics

We now turn to eqn (A.13) to assess the elasto-hydrodynamic balance that sets the gap height in both cases, long and short cells, highlighted above. When differentiated with respect to z,
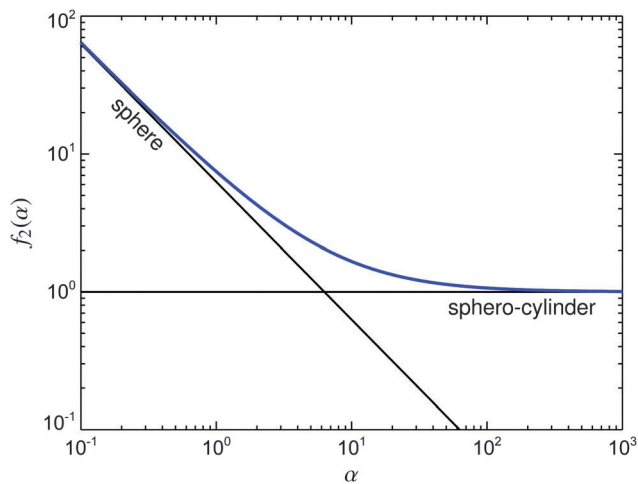
Fig. 4 Plot of the function $f_2(\alpha) = 1 + \frac{2\pi}{\alpha} + \frac{\pi}{3\pi + 8\alpha}$ (blue), characterizing the dependency of the cell dynamics on its shape in the tube. The two limits, $\frac{2\pi}{\alpha}$ for $\alpha \ll \alpha_c$ and 1 for $\alpha \gg \alpha_c$ correspond to spherical and sphero-cylindrical cell shape, respectively. We observe that $\alpha_c \sim 10$.

eqn (A.13) reads

$$t_0 \frac{d^3 h}{dz^3} = -\frac{dp}{dz}, \qquad (A.23)$$

where we have assumed that t_0 is uniform in the membrane and $t_0 \gg \tau$. If we call η the characteristic variation of h over a characteristic distance λ, the left side of the equation scales as $t_0 \frac{d^3 h}{dz^3} \sim \frac{t_0 \eta}{\lambda^3}$. Equating this with the pressure gradient $-\frac{dp}{dz} \sim \frac{\mu u \eta}{h^3}$, obtained using the lubrication approximation in the gap, eqn (A.12), implies that

$$h \sim \lambda \text{Ca}^{1/3}. \qquad (A.24)$$

Similar scalings have been proposed to support the simulation studies of comparable systems.[42,43]

For a long cell ($\ell \gg r$), the clearance has a constant value except near the spherical ends, where the dominating pressure drop occurs. At the cell ends, $\eta = h$ and the curvature $\frac{h}{\lambda^2} \sim \frac{1}{r}$, so that $\lambda \sim \sqrt{hr}$, typical for a spherical contact. Eqn (A.24) then yields $\varepsilon = \frac{h}{r} \sim \text{Ca}^{2/3}$, the classical Bretherton scaling for long bubbles.[35,44,45] For shorter cells, $\lambda \sim \ell$ and we derive the alternate scaling law $\varepsilon \sim \frac{\ell}{r} \text{Ca}^{1/3}$.

We expect that the length of the cell at which the transition between these two elasto-hydrodynamic regimes occurs is the same as the purely hydrodynamic transition length ℓ_c calculated in the previous section. Hence, we finally obtain

$$\varepsilon \sim \begin{cases} \text{Ca}^{2/3} & \text{for } \ell > \ell_c, \\ \frac{\ell}{r} \text{Ca}^{1/3} & \text{for } \ell < \ell_c, \end{cases} \qquad (A.25)$$

with $\ell_c \sim 10\sqrt{2hr}$.

References

1 A. S. Popel and P. C. Johnson, *Annu. Rev. Fluid Mech.*, 2005, **37**, 43.
2 A. R. Pries and T. W. Secomb, *Am. J. Physiol.: Heart Circ. Physiol.*, 2005, **289**, H2657.
3 J. H. Jeong, Y. Sugii, M. Minamiyama and K. Okamoto, *Microvasc. Res.*, 2006, **71**, 212.
4 R. M. Hochmuth, R. N. Marple and S. P. Sutera, *Microvasc. Res.*, 1970, **2**, 409.
5 M. Abkarian, M. Faivre, R. Horton, K. Smistrup, C. A. Best-Popescu and H. A. Stone, *Biomed. Mater.*, 2008, **3**, 034011.
6 G. Tomaiuolo, M. Simeone, V. Martinelli, B. Rotoli and S. Guido, *Soft Matter*, 2009, **5**, 3736.
7 A. R. Pries, D. Neuhaus and P. Gaehtgens, *Am. J. Physiol.: Heart Circ. Physiol.*, 1992, **263**, H1770.
8 S. Chien, *Annu. Rev. Physiol.*, 1987, **49**, 177.
9 T. W. Secomb, R. Skalak, N. Özkaya and J. F. Gross, *J. Fluid Mech.*, 1986, **163**, 405.
10 S. Guido and G. Tomaiuolo, *C. R. Phys.*, 2009, **10**, 751.
11 G. R. Lázaro, A. Hernández-Machado and I. Pagonabarraga, *Soft Matter*, 2014, **10**, 7195.
12 R. M. Hochmuth and R. E. Waugh, *Annu. Rev. Physiol.*, 1987, **49**, 209.
13 E. A. Evans and Y.-C. Fung, *Microvasc. Res.*, 1972, **4**, 335.
14 O. Linderkamp and H. J. Meiselman, *Blood*, 1982, **59**, 1121.
15 J. M. Higgins, D. T. Eddington, S. N. Bhatia and L. Mahadevan, *Proc. Natl. Acad. Sci. U. S. A.*, 2007, **104**, 20496.
16 D. K. Wood, A. Soriano, L. Mahadevan, J. M. Higgins and S. N. Bhatia, *Sci. Transl. Med.*, 2012, **4**, 123ra26.
17 A. M. Dondorp, E. Pongponratn and N. J. White, *Acta Trop.*, 2004, **89**, 309.
18 J. P. Shelby, J. White, K. Ganesan, P. K. Rathod and D. T. Chiu, *Proc. Natl. Acad. Sci. U. S. A.*, 2003, **100**, 14618.
19 T. W. Secomb, *Microvasc. Res.*, 1987, **34**, 46.
20 As to most formulas presented in the article, we refer to the Appendix for a detailed derivation.
21 G. K. Batchelor, *An Introduction to Fluid Dynamics*, Cambridge University Press, Cambridge, UK, 2000.
22 M. R. Nejadnik, A. L. J. Olsson, P. K. Sharma, H. C. van Der Mei, W. Norde and H. J. Busscher, *Langmuir*, 2009, **25**, 6245.
23 J. R. Henriksen and J. H. Ipsen, *Eur. Phys. J. E: Soft Matter Biol. Phys.*, 2004, **14**, 149.
24 R. D. Purves, *Biophys. J.*, 1980, **29**, 523.

25 E. Ponder, *Hemolysis and related phenomena*, Grune & Stratton, New York, reissued edn, 1971.

26 Y.-C. Fung, *Biomechanics: Circulation*, Springer, New York, 2nd edn, 1996.

27 P. Vennemann, R. Lindken and J. Westerweel, *Exp. Fluids*, 2007, **42**, 495.

28 E. A. Evans, R. E. Waugh and L. Melnik, *Biophys. J.*, 1976, **16**, 585.

29 R. M. Hochmuth, *J. Biomech.*, 2000, **33**, 15.

30 H. Byun, T. R. Hillman, J. M. Higgins, M. Diez-Silva, Z. Peng, M. Dao, R. R. Dasari, S. Suresh and Y. Park, *Acta Biomater.*, 2012, **8**, 4130.

31 E. A. Evans and R. E. Waugh, *Biophys. J.*, 1977, **20**, 307.

32 J. N. Israelachvili, *Intermolecular and Surface Forces*, Academic Press, San Diego, 3rd edn, 2011.

33 G. F. Teletzke, *Thin liquid films: molecular theory and hydrodynamic implications*, PhD thesis, University of Minnesota, Minneapolis, 1983.

34 Q. Zhang, K. S. Turitsyn and T. A. Witten, 2010, arXiv 1003.2732, http://arxiv.org/abs/1003.2732v1 1003.2732v1.

35 F. P. Bretherton, *J. Fluid Mech.*, 1961, **10**, 166.

36 R. E. Mebius and G. Kraal, *Nat. Rev. Immunol.*, 2005, **5**, 606.

37 T. Kong, L. Wang, H. M. Wyss and H. C. Shum, *Soft Matter*, 2014, **10**, 3271.

38 M. Mani, A. Gopinath and L. Mahadevan, *Phys. Rev. Lett.*, 2012, **108**, 226104.

39 S. P. Sutera, V. Seshadri, P. A. Croce and R. M. Hochmuth, *Microvasc. Res.*, 1970, **2**, 420.

40 R. M. Hochmuth and S. P. Sutera, *Chem. Eng. Sci.*, 1970, **25**, 593.

41 P. M. Bungay and H. Brenner, *Int. J. Multiphase Flow*, 1973, **1**, 25.

42 M. T. Kreutzer, F. Kapteijn, J. A. Moulijn, C. R. Kleijn and J. J. Heiszwolf, *AIChE J.*, 2005, **51**, 2428.

43 S. Kuriakose and P. Dimitrakopoulos, *Phys. Rev. E: Stat., Nonlinear, Soft Matter Phys.*, 2011, **84**, 011906.

44 R. F. Bruinsma, *Physica A*, 1996, **234**, 249.

45 D. Halpern and T. W. Secomb, *J. Fluid Mech.*, 1992, **244**, 307.